MXene-contacted Carbon Nanotube Thin-Film Transistors using Aerosol Jet Printing

Baiyu Zhang, *Student Member, IEEE*, Hansel A. Hobbie, *Student Member, IEEE*, Yizhang Wu, Wubin Bai, and Aaron D. Franklin*, *Fellow, IEEE*

Abstract— **MXenes have garnered significant attention for electronics applications due to their facile synthesis, tunable properties, and exceptional optical and electrical characteristics. Their stable aqueous suspension without additional surfactants enables compatibility of MXenes with various low-cost, additive manufacturing techniques, including spin coating, spraying, and direct-write printing. In this work, we investigate the aerosol jet printing of water-based $Ti_3C_2T_x$ MXene on surfaces with different wettability, achieving printed thin films with sheet resistance as low as ~7 Ω/□ within three printing passes on both hydrophilic and hydrophobic substrates. Furthermore, we present MXene-contacted carbon nanotube thin-film transistors (CNT-TFTs) with various device geometries, finding a tradeoff between on- and off-state performance when selecting between bottom and top contacts, respectively. Devices with MXene contacts exhibited performance (on-state current up to 16.9 µA/mm and on/off-current ratio of 10^6) comparable to printed CNT-TFTs contacted by graphene and silver nanowires; meanwhile, the lower unit price of MXene ink makes it a more attractive candidate for low-cost, large-area fabrication.**

Index Terms— **Aerosol jet printing, printed circuits, carbon nanotubes, additive manufacturing, semiconductor devices, nanomaterials.**

I. INTRODUCTION

THE Internet of Things (IoT) is ushering in a future in which everyday objects, from household appliances to healthcare devices, are equipped with electronics that enable the automatic collection, sharing, and analysis of data [1], [2]. To meet the demand for IoT, a broad range of devices are needed, including thin-film transistors (TFTs) for driving custom display interfaces, supporting flexible electronics platforms, and enabling new sensing modalities [3]-[5]. Given the long-term goal of ubiquity for IoT devices, the costs for materials and manufacturing must be as low as possible. Traditional silicon transistor technology falls short of meeting these various needs due to inherent limitations such as poor mechanical flexibility, high customization costs, and limited material compatibility. These limitations have spurred extensive research over the past two decades into novel additive manufacturing techniques [6]-[11] and alternative electronic materials [12]-[17].

Aerosol jet printing (AJP), an advanced additive manufacturing technique, is gaining significant traction in the research community for its suitability in the scalable, large-area fabrication of TFTs [18]-[22]. Recent demonstrations of fully printed devices with AJP have included carbon-based recyclable TFTs [23], microfluidic devices [24], photodetectors [25], immunosensors [26], and memristive bioelectronics [27]. The AJP method offers numerous advantages over other direct-write printers, including high resolutions (~10µm), minimal material wastage, precise deposition control, and compatibility with a variety of solution-based materials and substrates. Additionally, AJP allows for ready customization in pattern design and material selection, enabling the exploration of innovative insulating, semiconducting, and conducting materials for TFT printing.

Two-dimensional transition metal carbides and nitrides, collectively known as MXenes, have emerged as promising conductive materials in the field of printed electronics [28]. The synthesizing of MXenes involves the exfoliation of their precursor MAX phases, where M represents an early transition metal, A is an element from groups IIIA or IVA, and X is either carbon (C) or nitrogen (N). After a chemical etchant selectively removes the A element, the disassembled $M_{n+1}X_n$ framework results in a layered structure adorned with surface termination groups such as -O, -OH, and -F [29]. These surface termination groups impart a highly negative charge, enabling the stable dispersion of MXene in various solvents at concentrations ranging from a few to hundreds of mg/mL without additional modifiers [30]. $Ti_3C_2T_x$, the most extensively studied MXene, has been widely investigated for applications including micro-supercapacitors [31]-[33], optoelectronics [34], [35], biomedical sensors [36], [37], temperature and force sensors [38], [39], and electromagnetic interference shielding [40], [41] owing to its distinct optical and electrical properties.

Despite the significant advantages of $Ti_3C_2T_x$ in electrical properties and water solubility, research on TFT applications utilizing MXenes as electrode contacts remains sparse. Although there have been reports of using exfoliated $Ti_3C_2T_x$ flakes as contacts for TFTs, the completion of transistor

---

Manuscript received on XX, XX, 2024; accepted on XX, XX, 2024. Date of publication XX, XX, 2024. This work was supported by the National Science Foundation under grant No. FuSe-2328712 and EPMD-2227175. *(Corresponding author: Aaron D. Franklin.)*

Baiyu Zhang, and Hansel A. Hobbie are with the Department of Electrical and Computer Engineering, Duke University, Durham, NC, 27708, USA (e-mail: baiyu.zhang@duke.edu)

Aaron D. Franklin is with the Department of Chemistry and the Department of Electrical and Computer Engineering, Duke University, Durham, NC, 27708, USA (e-mail: aaron.franklin@duke.edu)

Yizhang Wu and Wubin Bai are with the Department of Applied Physical Sciences, the University of North Carolina at Chapel Hill, Chapel Hill, NC, 27599, USA (e-mail: wbai@unc.edu)

fabrication required additional lithography and metal deposition steps [42]-[44]. A few studies have reported the use of large-area deposition methods, such as spin coating and spraying; however, these approaches often require numerous deposition cycles and high-temperature post-process annealing to eliminate residual solvents to achieve adequately conductive films [45]-[47]. There are limited demonstrations of aerosol jet-printed MXene but they focused on mixed electrodes (rather than pure MXene) such as MXene/hydrogel composite [36], mixed graphene-MXene (singular MXene electrode) [38], and hybridization of MXene with carbon nanospheres [48]. Opportunities for AJP of pure MXene inks are worth exploring along with its use in thin-film transistors.

In this study, we present the deposition of a water-based $Ti_3C_2T_x$ MXene ink using an aerosol jet printer at low processing temperatures (≤ 60 °C) and investigate the impact of printing parameters, including platen temperature during printing, printing passes, and surface wettability, on the formation and quality of thin films. Additionally, we demonstrate the fabrication compatibility of water-based MXene ink with a toluene-based CNT ink and evaluate the performance of MXene-contacted carbon nanotube thin-film transistors (CNT-TFTs) with different contact geometries. Our results also show that MXene-contacted transistors exhibit performance comparable to transistors contacted with silver nanowires and graphene.

II. EXPERIMENTAL DETAILS

All printing in this study was conducted using an Optomec AJ300 aerosol jet printer, with a nozzle diameter of 150 µm and a printing speed of 2 mm/s. The MXene used in this work was purchased from Feynman Nano at a 10 mg/mL concentration and used without additional modification. The CNT ink was purchased from NanoIntegris (IsoSol-S100) and further diluted with toluene to a 0.01 mg/mL concentration.

To examine the impact of surface wettability on printing results, a silicon substrate with p-doped silicon and a 90 nm SiO_2 layer was used to represent a hydrophilic surface, and an ~8 µm thick parylene film deposited onto a separate silicon wafer was used to represent a hydrophobic surface. Both substrates underwent a cleaning procedure involving triple deionized water rinsing and nitrogen gas drying before AJP. To eliminate the impact on film quality due to other printer parameters, atomizer flow and sheath flow - key parameters in the printing process - were kept at 25 and 22 sccm, respectively, across all samples to ensure consistency. Only the atomizer current that controls aerosolization was adjusted to optimize ink performance under varying printing conditions. Rectangular patterns, measuring 0.5 mm by 4 mm and containing 23 lines printed in a serpentine arrangement, were designed for this experiment. The rectangles were systematically printed onto both SiO_2 and parylene substrates, with the platen heated to 20 °C, 40 °C, and 60 °C. Additionally, at each platen temperature, the number of printing passes for the samples was varied from 1 to 3 layers to assess the stacking of printed MXene. Subsequent electrical characterization measuring the sheet resistance of printed thin films was conducted using a Signatone benchtop probe station. Water contact angle (WCA) measurements were conducted by dropping a 2µL water droplet onto each substrate, and the contact angles were measured using an optical microscope. The thickness of these printed films was measured with a KEYENCE VK-X3000 3D Surface Profiler, and data was further analyzed and plotted into 3D mapping on KEYENCE software.

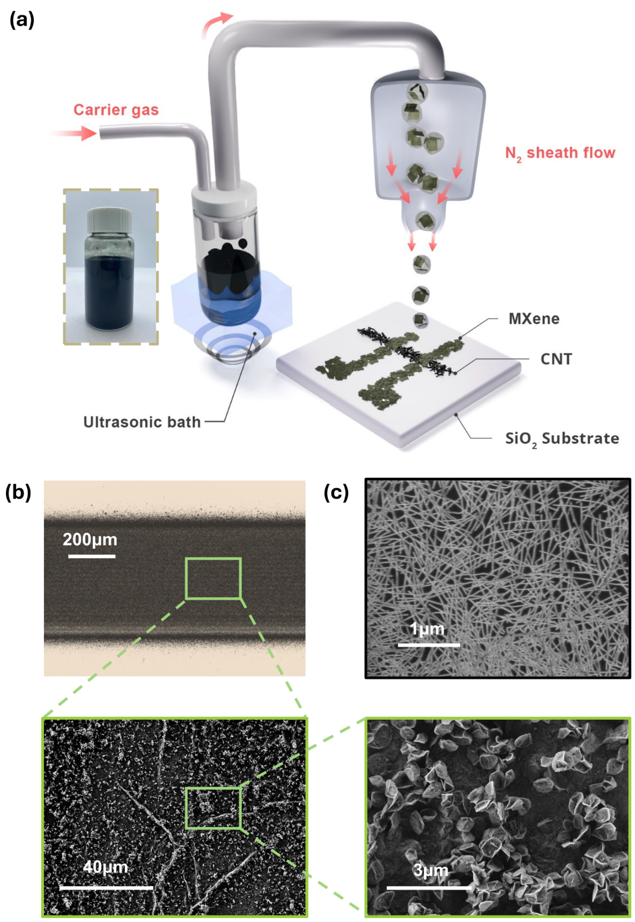

Fig. 1. Schematic of aerosol jet printed MXene thin films. (a) Illustration of aerosol jet printer depositing MXene-contacted CNT-TFT devices with an inset showing the aqueous MXene ink. (b) Optical microscopy and SEM images of the printed MXene thin films showing the microstructure of MXene particles. (c) SEM image showing printed CNT thin-film channel.

In the experiments investigating and benchmarking MXene-contacted CNT-TFTs, all devices were fabricated on p+ doped Si wafers with a thermally grown 90 nm SiO_2 layer serving as the back-gate dielectric. Prior to material deposition via AJP, wafers underwent a thorough cleaning procedure involving sonication in isopropyl alcohol (IPA) and acetone baths for 10 minutes each. Standardized device designs featuring both channel length (L_{ch}) and width (W_{ch}) of 200 µm were employed to ensure consistent comparison across all devices. All MXene electrodes were printed on the substrate heated to 60°C without post-deposition sintering. CNTs were printed onto the substrate at 20°C, followed by a 10-minute rinse in toluene to remove any polymeric binders left from the CNT deposition. Graphene ink used in this study was purchased from Sigma-Aldrich (808261) with a concentration of 100 mg/mL and further diluted with deionized (DI) water at a 1:2 ratio before printing. AgNW ink was also purchased from Sigma-Aldrich (806617) with a concentration of 5 mg/mL suspended in ethanol and used as-is. Three contact materials were deposited as single-pass bottom contacts with CNT printed atop as channels. Electrical characterization was performed using a benchtop probe station and Keysight B2902A analyzer.

III. RESULTS AND DISCUSSIONS

A schematic of the AJP process used for depositing MXene as TFT electrodes is shown in Fig. 1(a), with an inset displaying the bottle of commercial $Ti_3C_2T_x$ ink. During the AJP process, the MXene ink in the ultrasonic bath is atomized into an aerosol mist. A carrier gas flow then transports the aerosolized droplets to the deposition head, where a sheath flow jets the ink stream out of the nozzle tip, focusing it onto the target substrate. Optical microscopy and scanning electron microscopy (SEM) images of the MXene thin films printed on a SiO_2 substrate heated to 40°C (via the printer platen) are shown at various magnifications in Fig. 1(b). The SEM images reveal that the morphology of the printed MXene particles resembles crumpled nanospheres rather than 2D nanosheets. This morphology is attributed to the Marangoni effect induced by the heated substrate and the inward capillary force compression from the evaporating solvent causing the nanosheets to bend upward during the deposition process [49].

The impact of surface wettability on water-based MXene printing was explored using SiO_2 and parylene substrates. Previous studies have demonstrated that the resistance of MXene has a pronounced temperature dependence, leading to the use of MXene in temperature sensors [50]. Considering this temperature-dependent electrical property of MXene, this study employed a heated platen to vary substrate temperatures during the MXene printing process, followed by sheet resistance measurements conducted after the samples cooled to room temperature. As illustrated in Fig. 2(a), a clear inverse correlation was observed between platen temperature and the resultant sheet resistance of the printed films. Specifically, on parylene substrate with 1 printing pass, the sheet resistance of the MXene films decreased by 92%, from 223.8 Ω/□ to 17.5 Ω/□, as the platen temperature was increased from 20 °C to 60 °C during printing. This can be explained by elevated substrate temperatures facilitated accelerated solvent evaporation upon impingement of aerosolized droplets to the substrate surface, thereby promoting the removal of water molecules trapped among MXene particles and leading to enhanced particle adhesion and stacking, which consequently resulted in decreased sheet resistance. Similarly, samples printed on SiO_2 exhibited a comparable dependence on platen temperature during printing, with sheet resistance decreasing from 122.2 Ω/□ to 13.2 Ω/□ (an 89% reduction) as temperature varied from 20 °C to 60 °C. Notably, samples on SiO_2 substrates demonstrated an overall lower sheet resistance than samples on parylene as the hydrophilic nature of SiO_2 improved the adhesion of ink droplets and the formation of MXene films.

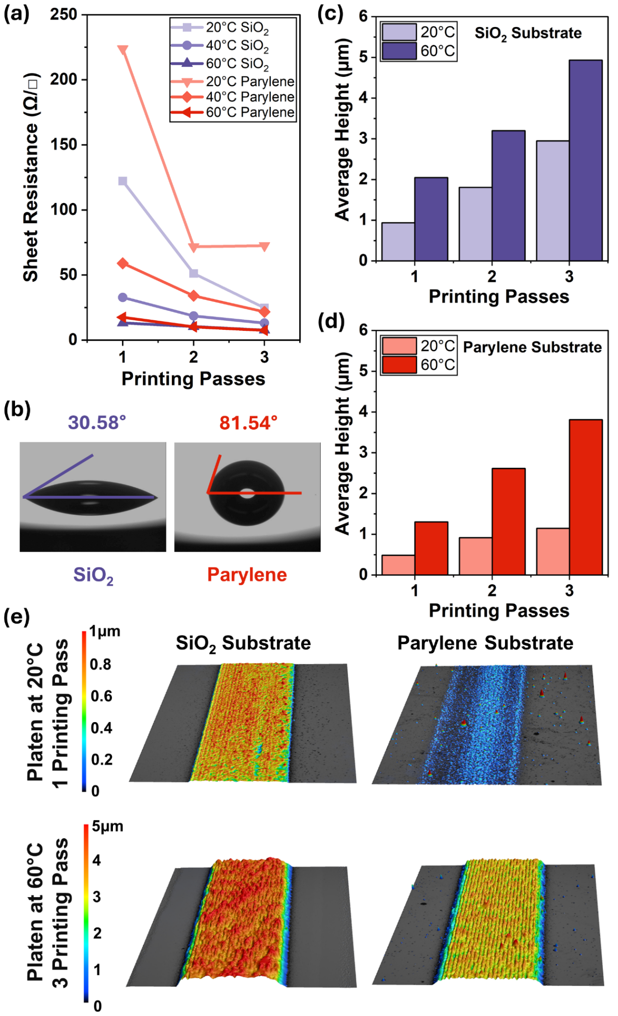

Fig. 2. Characterization of aerosol jet printed MXene thin films on surfaces of different wettability. (a) Sheet resistance of printed MXene films on SiO_2 and parylene substrates with varied platen temperatures and 1 to 3 print passes. (b) Water contact angle (WCA) on SiO_2 (hydrophilic) and parylene (hydrophobic) substrates. Profilometry measurement of printed MXene film thickness under various printing parameters on (c) SiO_2 and (d) parylene. (e) 3D mapping of MXene thin films printed on SiO_2 and parylene substrates where samples in the top row were printed with 1 printing pass on 20 °C substrates and samples in the bottom row were printed with 3 printing passes on 60°C substrates. The mapping profile was enlarged in z-direction for better visualization.

Sheet resistance of the printed MXene thin films decreased with increasing printing passes irrespective of substrate material, indicative of improved thin-film coverage from greater material deposition. Interestingly, the influence of printing passes was more pronounced at lower substrate temperatures during printing. For instance, on SiO_2 substrates at 20 °C, sheet resistance decreased from 122.2 $\Omega/\square$ to 51.1 $\Omega/\square$ and further to 24.8 $\Omega/\square$ with 1, 2, and 3 printing passes, respectively. Conversely, on SiO_2 substrates at 40 °C and 60 °C, diminishing returns were observed with increasing printing passes. A similar trend was also observed on samples printed on parylene substrates. This observation highlighted the dominating effect that substrate heating has on film formation and resulting resistivity, independent of the substrate materials.

In contrast to prior studies that required a substantial number of deposition cycles to achieve low resistance [47], [50], this study applied only 3 printing passes to achieve a remarkably low sheet resistance of approximately ~7.5 $\Omega/\square$ for MXene samples printed on SiO_2 and parylene substrates at 60 °C. WCA measurements were conducted on SiO_2 (left) and parylene (right) surfaces, as depicted in Fig. 2(b). The comparatively smaller water contact angle on SiO_2 facilitates a more uniform spreading of MXene droplets across the substrate, which improves the stacking of MXene to form a cohesive thin film. Due to this difference in WCA between the two substrates, the thickness of printed films was consistently larger on the SiO_2 as opposed to the parylene, as shown in Fig. 2(c-d). This disparity in film thickness can be attributed to the hydrophilic nature of SiO_2 as opposed to parylene, where prolonged solvent evaporation was observed due to the surface tension of water on the hydrophobic surface. This effect caused thinning of the MXene deposition since subsequently printed lines in the serpentine pattern often overlapped with previous lines that had yet to evaporate, causing the spreading of the deposited ink. Therefore, platen temperature during printing had a more pronounced influence on film thickness for parylene samples than SiO_2 samples because of the improved evaporation at elevated temperatures.

Fig. 2(e) offers a comprehensive portrayal of surface topology as well as the impact of substrate temperature and printing passes via three-dimensional (3D) mapping of thin films, with color denoting film thickness at any given point. Films were printed with 1 pass on substrates at 20°C and with 3 passes on substrates at 60°C under identical printing conditions. SiO_2-supported films exhibited superior uniformity and coverage compared to films on the parylene substrate, which agreed with the observed lower sheet resistance for films on SiO_2. Additionally, the 3D mapping revealed that platen heating during printing effectively enhanced the resolution of the printed patterns through mitigated overspray by reducing redispersion.

These printed MXene thin films were also explored as contact electrodes in CNT transistors with various device architectures. Carbon nanotubes were chosen as the channel material as they have demonstrated excellent thin-film transistor performance when deposited using AJP [23], [51]-[55]. MXene source and drain electrodes were deposited on 60°C SiO_2 based on the satisfactory conductivity of the as-printed films and the effectiveness of printing on heated substrates in reducing overspray in the channel region.

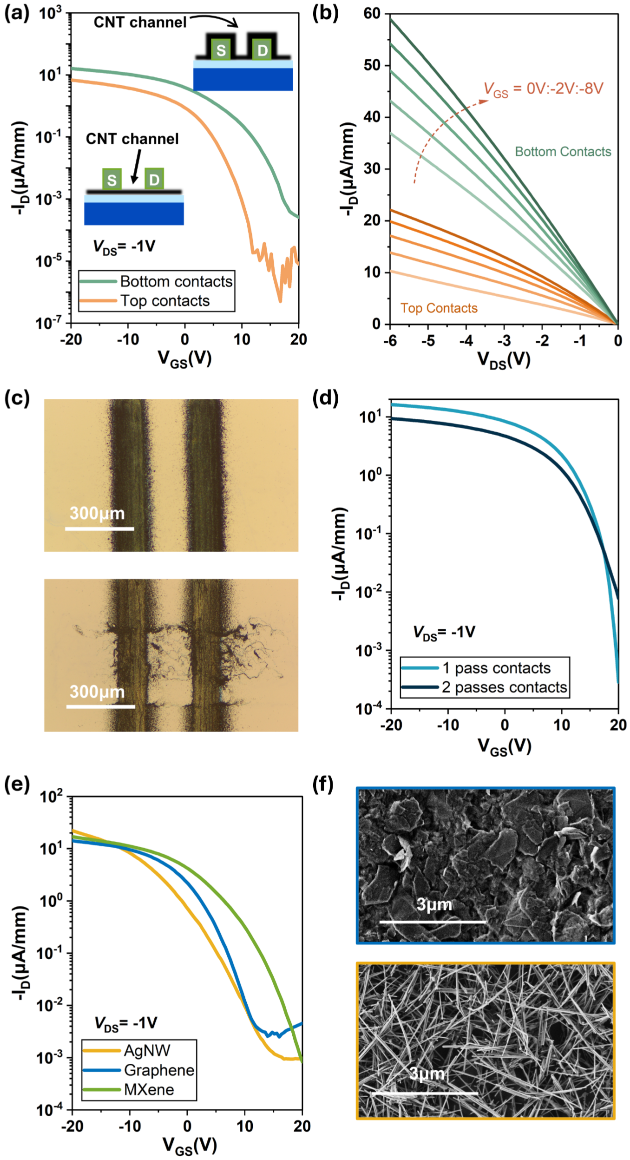

Fig. 3. Printed MXene-contacted CNT-TFTs of various device geometries. (a) Subthreshold and (b) output characterization of bottom- and top-contacted CNT-TFTs with insets depicting device structure schematics. (c) Optical microscopy image of bottom-contacted CNT-TFTs without (top) and with (bottom) undesired redispersion of MXene electrodes after CNT printing process. (d) Subthreshold characteristics of bottom-contacted CNT-TFTs with electrodes printed by 1 pass and 2 passes. (e) Subthreshold characteristics of CNT-TFTs with printed AgNW, graphene, and MXene electrodes. (f) SEM images of printed graphene (top) and AgNW (bottom) electrodes under high magnification. The channel length of all TFTs was 200 μm.

First, top- and bottom-contacted devices were fabricated, and their performance was compared and analyzed. The insets of Fig. 3(a) depict the difference in the two device structures. For bottom-contacted devices, MXene was deposited first to define the source and drain electrodes as well as alignment marks, followed by the deposition of CNTs over the contacts in the designated area. On the other hand, top-contacted devices feature direct deposition of CNTs onto SiO_2 followed by printing MXene electrodes onto the CNT channel. Note that in top-contacted configuration, since CNT thin films are invisible under the optical microscope, an additional printing step is needed before CNT deposition to define alignment marks. In both configurations, MXene electrodes were printed using a single pass.

Transistor characterization, as shown in Fig. 3(a), revealed that the bottom-contacted TFT exhibited an on-current (I_{ON}) of 16.15 μA/mm - over twice as high as that of the top-contacted device (6.85 μA/mm). However, the top-contacted device exhibited an on/off-current ratio (I_{ON}/I_{OFF}) of ~10^6, compared to ~10^5 for the bottom-contacted counterpart. In the top-contacted structure, the CNT network is deposited on the flat SiO_2 substrate, resulting in a more intimate interface with the gate, which also modulates the CNT thin film beneath the contacts. However, in the bottom-contacted configuration, the MXene contacts were approximately 2 μm thick, posing challenges for the formation of a thin CNT network that was printed atop the contacts. Additionally, the presence of MXene electrodes in the bottom-contacted device could impede liquid flow during the rinsing process, hindering the removal of polymer residue in the CNT films and contributing to a non-uniform network in the channel areas. Output characteristics for the TFTs are shown in Fig. 3(b). Under small gate fields, the bottom-contacted device consistently outperformed the top-contacted device, displaying higher transconductance.

Moreover, although rinsing in toluene did not result in the complete dissolution of MXene electrodes, there remains a potential risk of redispersing MXene particles when printing CNTs atop. During the fabrication of bottom-contacted devices, the solvent present in CNT droplets and the jetting force from the AJP nozzle can potentially redisperse and redistribute the deposited MXene material, introducing undesired conductive MXene nanoparticles into the channel area. Fig. 3(c) presented two bottom-contacted devices, where one device had intact contacts after CNT deposition (top), and the other showed clear evidence of MXene being redispersed and introduced into the channel area (bottom) after printing CNTs. The occurrence of undesirable MXene redispersion can be attributed to weaker adhesion of MXene on substrates caused by unoptimized printing parameters, or an aggressive jetting of CNT solvent and sheath flow during the CNT deposition. By comparison, the top-contacted device - immune to the contact redispersion issue - exhibited an off-current (I_{OFF}) nearly two orders of magnitude lower than the bottom-contacted device, while the I_{ON} was only 57.6% lower. Hence, adopting a bottom-contacted structure saves one printing step and yields higher on-current, yet it carries the risk of redistributing underlying conductive materials into the channel, thereby degrading off-state performance. Conversely, the top-contacted design preserves the integrity of the channel area but necessitates an additional fabrication step.

Although increasing the number of MXene printing passes led to a significant decrease in series resistance in the electrode area, which is a component of the total resistance of transistor devices, as illustrated by the subthreshold characteristics of representative devices in Fig. 3(d), devices with bottom contacts printed with 1 pass had an overall better performance than the device with contacts printed with 2 passes. The 2-pass device displayed a much higher I_{OFF} and an I_{ON}/I_{OFF} of only ~10^3. The higher I_{OFF} in the 2-pass device could be attributed to the introduction of more MXene flakes into the channel area during the CNT printing process because of redispersion. Additionally, an increase in printing passes resulted in an increase in MXene film thickness from 2 μm to 3.2 μm for 1 and 2 passes, respectively. Previous studies have confirmed that printed CNT films typically possess a mean thickness of 9 nm [56], hence, the increase in thickness posed a larger barrier for CNT thin films to form good contact with the electrodes and planar gate substrate underneath. Furthermore, augmenting electrode thickness could exacerbate the non-uniformity of the CNT network during the rinsing process and lead to higher sheet resistance in the channel area. Thus, it is imperative to control the thickness of the printed contact electrodes. While a sufficiently thick film ensures the formation of a conductive network, excessively thick electrodes can elevate contact resistance and channel sheet resistance, which detrimentally impacts overall transistor performance.

To assess the performance of MXene-contacted transistors relative to devices employing more common contact materials, bottom-contacted devices featuring silver nanowire (AgNW) and graphene electrodes were also printed and characterized. These materials were chosen as benchmarks for MXene given their prior use as electrodes for printed TFTs and reported outstanding performance [18], [51]-[53], [57]. Ten devices for each contact material in the bottom-contact configuration were fabricated and measured with minimal variation in performance observed. The subthreshold characterization of one representative device for each contact material is presented in Fig. 3(e) and SEM of the printed AgNW and graphene films are provided in Fig. 3(f). As depicted in the subthreshold characterization, devices employing printed AgNW, graphene, and MXene contacts exhibited similar performance in terms of I_{ON}/I_{OFF} (~10^4) and I_{ON} (22.1, 14.2, and 16.9 μA/mm, respectively). Table 1 provides a more detailed benchmark comparison of device performance and fabrication parameters for aerosol jet-printed MXene-contacted CNT-TFTs with other TFTs contacted by AgNW and graphene reported in the literature. This comparison highlights the low-cost advantage of printed MXene electrodes while still delivering competitive performance in CNT-TFTs at a low overall processing temperature.

On a more qualitative note, beyond having comparable device performance, MXene also exhibited preferential compatibility with the printing process when compared to AgNW and graphene. Due to its high aspect ratio which poses a greater challenge in aerosolization and droplet formation,

TABLE I
BENCHMARK COMPARISON OF TFT PERFORMANCE USING AGNW, GRAPHENE, AND MXENE AS CONTACTS

Ref.	Channel Material	Electrode Material	Fabrication Method	Electrode Cost ($/g)	V_{DS} (V)	I_{ON} (µA/mm)	Best I_{ON}/I_{OFF}	Processing Temperature (°C)
[55]	CNT	AgNW	AJP	(Synthesized)	-1	0.52	3.5×10^5	80
[23]	CNT	Graphene	AJP	$1053	-0.5	87	10^3-10^4	RT
[44]	MoS_2	MXene	Spin coat	(Synthesized)	1	10*	10^5	RT
[47]	In_2O_3/ZnO	MXene	Spray coat	(Synthesized)	2	121	10^4	150
This work	CNT	AgNW	AJP	$3896	-1	22.1	2.3×10^4	RT
This work	CNT	Graphene	AJP	$702	-1	14.2	5.7×10^3	RT
This work	CNT	MXene	AJP	$276	-1	16.9	3.4×10^6	60

*This current is reported in µA as the device dimension was not given.

AgNW ink often requires delicate tuning before the printing procedure can initiate. Graphene ink has a high viscosity which necessitates long preconditioning in an ultrasonic bath for ink to reach a stable, uniform solution. However, due to the lower ink concentration and nanosheet structure in suspension, the MXene ink can be quickly aerosolized when loaded in the printer and little tuning effort is required for the printing process to begin. Moreover, commercial MXene has a unit price of $276/g, ~2.5x cheaper than graphene and ~14x cheaper than AgNW used in this study, making MXene a more economical candidate for electrode materials of low-cost and large-area applications, as shown in Table 1.

IV. CONCLUSION

Aerosol jet-printed MXene thin films have been shown to form good electrodes for fully printed CNT-TFTs. The water-based MXene ink was able to be printed onto both hydrophilic and hydrophobic substrates with low sheet resistance in the as-printed films. MXene-contacted CNT-TFTs of different device geometries were explored, revealing the impact of the fabrication procedure when printing the channel and contact layers. Notably, in bottom-contacted devices, although thicker electrodes aid in forming more conductive and well-covered films, they also impede effective contact between the CNT network and the underlying electrode. This leads to increased contact resistance and non-uniform channel sheet resistance, significantly compromising overall device performance. MXene-contacted devices demonstrated performance on par with those utilizing AgNWs and graphene. This parity encourages the application of MXene in low-cost, large-area printed electronics applications, such as optoelectronics, healthcare devices, and energy storage devices.

ACKNOWLEDGMENT

We acknowledge William Collins for assistance in creating the illustration in Fig. 1(a).

REFERENCES

[1] A. Khanna and S. Kaur, "Internet of Things (IoT), Applications and Challenges: A Comprehensive Review," Wireless Pers Commun, vol. 114, no. 2, pp. 1687–1762, Sep. 2020, doi: 10.1007/s11277-020-07446-4.

[2] R. A. Radouan Ait Mouha, "Internet of Things (IoT)," *J. Data Anal. Inf. Process.*, vol. 09, no. 02, pp. 77–101, 2021, doi: 10.4236/jdaip.2021.92006.

[3] R.-H. Kim *et al.*, "Stretchable, Transparent Graphene Interconnects for Arrays of Microscale Inorganic Light Emitting Diodes on Rubber Substrates," *Nano Lett.*, vol. 11, no. 9, pp. 3881–3886, Sep. 2011, doi: 10.1021/nl202000u.

[4] T. Varghese *et al.*, "High-performance and flexible thermoelectric films by screen printing solution-processed nanoplate crystals," *Sci. Rep.*, vol. 6, no. 1, p. 33135, Sep. 2016, doi: 10.1038/srep33135.

[5] C. D. Dimitrakopoulos and P. R. L. Malenfant, "Organic Thin Film Transistors for Large Area Electronics," *Adv. Mater.*, vol. 14, no. 2, pp. 99–117, Jan. 2002, doi: 10.1002/1521-4095(20020116)14:2<99::AID-ADMA99>3.0.CO;2-9.

[6] D. Song, A. Mahajan, E. B. Secor, M. C. Hersam, L. F. Francis, and C. D. Frisbie, "High-Resolution Transfer Printing of Graphene Lines for Fully Printed, Flexible Electronics," *ACS Nano*, vol. 11, no. 7, pp. 7431–7439, Jul. 2017, doi: 10.1021/acsnano.7b03795.

[7] J. Ding, F. T. Fisher, and E.-H. Yang, "Direct transfer of corrugated graphene sheets as stretchable electrodes," *J. Vac. Sci. Technol. B Nanotechnol. Microelectron. Mater. Process. Meas. Phenom.*, vol. 34, no. 5, p. 051205, Sep. 2016, doi: 10.1116/1.4961594.

[8] T.-H. Kim *et al.*, "Full-colour quantum dot displays fabricated by transfer printing," *Nat. Photonics*, vol. 5, no. 3, pp. 176–182, Mar. 2011, doi: 10.1038/nphoton.2011.12.

[9] W.-S. Liao, S. Cheunkar, H. H. Cao, H. R. Bednar, P. S. Weiss, and A. M. Andrews, "Subtractive Patterning via Chemical Lift-Off Lithography," *Science*, vol. 337, no. 6101, pp. 1517–1521, Sep. 2012, doi: 10.1126/science.1221774.

[10] F. Withers *et al.*, "Heterostructures Produced from Nanosheet-Based Inks," *Nano Lett.*, vol. 14, no. 7, pp. 3987–3992, Jul. 2014, doi: 10.1021/nl501355j.

[11] J. Zaumseil *et al.*, "Three-Dimensional and Multilayer Nanostructures Formed by Nanotransfer Printing," *Nano Lett.*, vol. 3, no. 9, pp. 1223–1227, Sep. 2003, doi: 10.1021/nl0344007.

[12] Y. Kumashiro, H. Nakako, M. Inada, K. Yamamoto, A. Izumi, and M. Ishihara, "Novel materials for electronic device fabrication using ink-jet printing technology," *Appl. Surf. Sci.*, vol. 256, no. 4, pp. 1019–1022, Nov. 2009, doi: 10.1016/j.apsusc.2009.05.134.

[13] K. Kang, Y. Cho, and K. Yu, "Novel Nano-Materials and Nano-Fabrication Techniques for Flexible Electronic Systems," *Micromachines*, vol. 9, no. 6, p. 263, May 2018, doi: 10.3390/mi9060263.

[14] B. Zhu *et al.*, "Microstructured Graphene Arrays for Highly Sensitive Flexible Tactile Sensors," *Small*, vol. 10, no. 18, pp. 3625–3631, Sep. 2014, doi: 10.1002/smll.201401207.

[15] S. Gong *et al.*, "Fabrication of Highly Transparent and Flexible NanoMesh Electrode via Self-assembly of Ultrathin Gold Nanowires," *Adv. Electron. Mater.*, vol. 2, no. 7, p. 1600121, Jul. 2016, doi: 10.1002/aelm.201600121.

[16] J. Zaumseil, C. L. Donley, J. -S. Kim, R. H. Friend, and H. Sirringhaus, "Efficient Top-Gate, Ambipolar, Light-Emitting Field-Effect Transistors Based on a Green-Light-Emitting Polyfluorene," *Adv. Mater.*, vol. 18, no. 20, pp. 2708–2712, Oct. 2006, doi: 10.1002/adma.200601080.

[17] A. J. Kell *et al.*, "Versatile Molecular Silver Ink Platform for Printed Flexible Electronics," *ACS Appl. Mater. Interfaces*, vol. 9, no. 20, pp. 17226–17237, May 2017, doi: 10.1021/acsami.7b02573.

[18] J. A. Cardenas, S. Lu, N. X. Williams, J. L. Doherty, and A. D. Franklin, "In-Place Printing of Flexible Electrolyte-Gated Carbon Nanotube Transistors with Enhanced Stability," *IEEE Electron Device Lett.*, vol. 42, no. 3, pp. 367–370, Mar. 2021, doi: 10.1109/LED.2021.3055787.

[19] K. Hong, S. H. Kim, A. Mahajan, and C. D. Frisbie, "Aerosol Jet Printed p- and n-type Electrolyte-Gated Transistors with a Variety of Electrode Materials: Exploring Practical Routes to Printed Electronics," *ACS Appl.*

Mater. Interfaces, vol. 6, no. 21, pp. 18704–18711, Nov. 2014, doi: 10.1021/am504171u.

[20]A. Mahajan, C. D. Frisbie, and L. F. Francis, "Optimization of Aerosol Jet Printing for High-Resolution, High-Aspect Ratio Silver Lines," *ACS Appl. Mater. Interfaces*, vol. 5, no. 11, pp. 4856–4864, Jun. 2013, doi: 10.1021/am400606y.

[21]L. Gamba, S. Diaz-Arauzo, M. C. Hersam, and E. B. Secor, "Aerosol Jet Printing of Phase-Inversion Graphene Inks for High-Aspect-Ratio Printed Electronics and Sensors," *ACS Appl. Nano Mater.*, p. acsanm.3c04207, Nov. 2023, doi: 10.1021/acsanm.3c04207.

[22]L. Kuo *et al.*, "All-Printed Ultrahigh-Responsivity MoS_2 Nanosheet Photodetectors Enabled by Megasonic Exfoliation," *Adv. Mater.*, vol. 34, no. 34, p. 2203772, Aug. 2022, doi: 10.1002/adma.202203772.

[23]N. X. Williams, G. Bullard, N. Brooke, M. J. Therien, and A. D. Franklin, "Printable and recyclable carbon electronics using crystalline nanocellulose dielectrics," *Nat. Electron.*, vol. 4, no. 4, pp. 261–268, Apr. 2021, doi: 10.1038/s41928-021-00574-0.

[24]J. Rich *et al.*, "Aerosol jet printing of surface acoustic wave microfluidic devices," *Microsyst. Nanoeng.*, vol. 10, no. 1, p. 2, Jan. 2024, doi: 10.1038/s41378-023-00606-z.

[25]A. A. Gupta, S. Arunachalam, S. G. Cloutier, and R. Izquierdo, "Fully Aerosol-Jet Printed, High-Performance Nanoporous ZnO Ultraviolet Photodetectors," *ACS Photonics*, vol. 5, no. 10, pp. 3923–3929, Oct. 2018, doi: 10.1021/acsphotonics.8b00829.

[26]K. Parate *et al.*, "Aerosol-Jet-Printed Graphene Immunosensor for Label-Free Cytokine Monitoring in Serum," *ACS Appl. Mater. Interfaces*, vol. 12, no. 7, pp. 8592–8603, Feb. 2020, doi: 10.1021/acsami.9b22183.

[27]R. Sajapin *et al.*, "Aerosol Jet Printed Organic Memristive Microdevices Based on a Chitosan:PANI Composite Conductive Channel," *ACS Appl. Electron. Mater.*, vol. 4, no. 12, pp. 5875–5883, Dec. 2022, doi: 10.1021/acsaelm.2c01047.

[28]M. Naguib *et al.*, "Two-Dimensional Nanocrystals Produced by Exfoliation of Ti_3AlC_2," *Adv. Mater.*, vol. 23, no. 37, pp. 4248–4253, Oct. 2011, doi: 10.1002/adma.201102306.

[29]O. Mashtalir *et al.*, "Intercalation and delamination of layered carbides and carbonitrides," *Nat. Commun.*, vol. 4, no. 1, p. 1716, Apr. 2013, doi: 10.1038/ncomms2664.

[30]Y. Zhang, Y. Wang, Q. Jiang, J. K. El-Demellawi, H. Kim, and H. N. Alshareef, "MXene Printing and Patterned Coating for Device Applications," *Adv. Mater.*, vol. 32, no. 21, p. 1908486, May 2020, doi: 10.1002/adma.201908486.

[31]Z. Wu, S. Liu, Z. Hao, and X. Liu, "MXene Contact Engineering for Printed Electronics," *Adv. Sci.*, vol. 10, no. 19, p. 2207174, Jul. 2023, doi: 10.1002/advs.202207174.

[32]Y. Zhu *et al.*, "Three-dimensional (3D) -printed MXene high-voltage aqueous micro-supercapacitors with ultrahigh areal energy density and low-temperature tolerance," *Carbon Energy*, p. e481, Mar. 2024, doi: 10.1002/cey2.481.

[33]D. Wen *et al.*, "Inkjet Printing Transparent and Conductive MXene ($Ti_3C_2T_x$) Films: A Strategy for Flexible Energy Storage Devices," *ACS Appl. Mater. Interfaces*, vol. 13, no. 15, pp. 17766–17780, Apr. 2021, doi: 10.1021/acsami.1c00724.

[34]K. Montazeri, M. Currie, L. Verger, P. Dianat, M. W. Barsoum, and B. Nabet, "Beyond Gold: Spin-Coated Ti_3C_2-Based MXene Photodetectors," *Adv. Mater.*, vol. 31, no. 43, p. 1903271, Oct. 2019, doi: 10.1002/adma.201903271.

[35]H. Vadakke Neelamana, S. M. Rekha, and S. V. Bhat, "$Ti_3C_2T_x$ MXene: A New Promising 2D Material for Optoelectronics," *Chem. Mater.*, vol. 35, no. 18, pp. 7386–7405, Sep. 2023, doi: 10.1021/acs.chemmater.3c01660.

[36]G. Basara *et al.*, "Electrically conductive 3D printed $Ti_3C_2T_x$ MXene-PEG composite constructs for cardiac tissue engineering," *Acta Biomater.*, vol. 139, pp. 179–189, Feb. 2022, doi: 10.1016/j.actbio.2020.12.033.

[37]A. Saleh *et al.*, "Inkjet-printed $Ti_3C_2T_x$ MXene electrodes for multimodal cutaneous biosensing," *J. Phys. Mater.*, vol. 3, no. 4, p. 044004, Oct. 2020, doi: 10.1088/2515-7639/abb361.

[38]M. Saeidi-Javash *et al.*, "All-Printed MXene–Graphene Nanosheet-Based Bimodal Sensors for Simultaneous Strain and Temperature Sensing," *ACS Appl. Electron. Mater.*, vol. 3, no. 5, pp. 2341–2348, May 2021, doi: 10.1021/acsaelm.1c00218.

[39]Z. Cao *et al.*, "Highly flexible and sensitive temperature sensors based on $Ti_3C_2T_x$ (MXene) for electronic skin," *J. Mater. Chem. A*, vol. 7, no. 44, pp. 25314–25323, 2019, doi: 10.1039/C9TA09225K.

[40]M. Han *et al.*, "Beyond $Ti_3C_2T_x$: MXenes for Electromagnetic Interference Shielding," *ACS Nano*, vol. 14, no. 4, pp. 5008–5016, Apr. 2020, doi: 10.1021/acsnano.0c01312.

[41]F. Shahzad *et al.*, "Electromagnetic interference shielding with 2D transition metal carbides (MXenes)," *Science*, vol. 353, no. 6304, pp. 1137–1140, Sep. 2016, doi: 10.1126/science.aag2421.

[42]J. Xu, J. Shim, J. Park, and S. Lee, "MXene Electrode for the Integration of WSe_2 and MoS_2 Field Effect Transistors," *Adv. Funct. Mater.*, vol. 26, no. 29, pp. 5328–5334, Aug. 2016, doi: 10.1002/adfm.201600771.

[43]S. Lai, S. K. Jang, J. H. Cho, and S. Lee, "Organic field-effect transistors integrated with Ti_2CT_x electrodes," *Nanoscale*, vol. 10, no. 11, pp. 5191–5197, 2018, doi: 10.1039/C7NR08677F.

[44]R. Chen *et al.*, "MoS_2 Transistor with Weak Fermi Level Pinning via MXene Contacts," *Adv. Funct. Mater.*, vol. 32, no. 43, p. 2204288, Oct. 2022, doi: 10.1002/adfm.202204288.

[45]X. Xu *et al.*, "High-Yield $Ti_3C_2T_x$ MXene–MoS_2 Integrated Circuits," *Adv. Mater.*, vol. 34, no. 48, p. 2107370, Dec. 2022, doi: 10.1002/adma.202107370.

[46]X. Tang *et al.*, "Engineering Aggregation-Resistant MXene Nanosheets As Highly Conductive and Stable Inks for All-Printed Electronics," *Adv. Funct. Mater.*, vol. 31, no. 29, p. 2010897, Jul. 2021, doi: 10.1002/adfm.202010897.

[47]E. Yarali *et al.*, "Fully Sprayed Metal Oxide Transistors Utilizing $Ti_3C_2T_x$ MXene Contacts," *ACS Appl. Electron. Mater.*, vol. 5, no. 2, pp. 784–793, Feb. 2023, doi: 10.1021/acsaelm.2c01286.

[48]Y. Wu *et al.*, "Aerosol Jet Printing of Hybrid $Ti_3C_2T_x$/C Nanospheres for Planar Micro-supercapacitors," *Front. Chem.*, vol. 10, p. 933319, Jul. 2022, doi: 10.3389/fchem.2022.933319.

[49]Y. Wu *et al.*, "Crumpled and Eccentric Nanospheres of $Ti_3C_2T_x$ MXene by Aerosol Jet Printing on Heat Substrate," *Adv. Eng. Mater.*, vol. 24, no. 8, p. 2101556, Aug. 2022, doi: 10.1002/adem.202101556.

[50]M. Borghetti, M. Serpelloni, E. Sardini, D. Spurling, and V. Nicolosi, "Temperature influence on $Ti_3C_2T_x$ lines printed by aerosol jet printing," *Sens. Actuators Phys.*, vol. 332, p. 113185, Dec. 2021, doi: 10.1016/j.sna.2021.113185.

[51]A. D. Franklin, M. C. Hersam, and H.-S. P. Wong, "Carbon nanotube transistors: Making electronics from molecules," *Science*, vol. 378, no. 6621, pp. 726–732, Nov. 2022, doi: 10.1126/science.abp8278.

[52]S. Lu and A. D. Franklin, "Printed carbon nanotube thin-film transistors: progress on printable materials and the path to applications," *Nanoscale*, vol. 12, no. 46, pp. 23371–23390, 2020, doi: 10.1039/D0NR06231F.

[53]S. Lu, J. Zheng, J. A. Cardenas, N. X. Williams, Y.-C. Lin, and A. D. Franklin, "Uniform and Stable Aerosol Jet Printing of Carbon Nanotube Thin-Film Transistors by Ink Temperature Control," *ACS Appl. Mater. Interfaces*, vol. 12, no. 38, pp. 43083–43089, Sep. 2020, doi: 10.1021/acsami.0c12046.

[54]J. A. Cardenas, J. B. Andrews, S. G. Noyce, and A. D. Franklin, "Carbon nanotube electronics for IoT sensors," *Nano Futur.*, vol. 4, no. 1, p. 012001, Jan. 2020, doi: 10.1088/2399-1984/ab5f20.

[55]S. Lu *et al.*, "Flexible, Print-in-Place 1D–2D Thin-Film Transistors Using Aerosol Jet Printing," *ACS Nano*, vol. 13, no. 10, pp. 11263–11272, Oct. 2019, doi: 10.1021/acsnano.9b04337.

[56]J. A. Cardenas, M. J. Catenacci, J. B. Andrews, N. X. Williams, B. J. Wiley, and A. D. Franklin, "In-Place Printing of Carbon Nanotube Transistors at Low Temperature," *ACS Appl. Nano Mater.*, vol. 1, no. 4, pp. 1863–1869, Apr. 2018, doi: 10.1021/acsanm.8b00269.

[57]D. McManus *et al.*, "Water-based and biocompatible 2D crystal inks for all-inkjet-printed heterostructures," *Nat. Nanotechnol.*, vol. 12, no. 4, pp. 343–350, Apr. 2017, doi: 10.1038/nnano.2016.281.